Contents lists available at ScienceDirect

Geomorphology

Characterizing Batagay megaslump topography dynamics and matter fluxes at high spatial resolution using a multidisciplinary approach of permafrost field observations, remote sensing and 3D geological modeling

Alexander I. Kizyakov [a,*], Maxim V. Korotaev [b], Sebastian Wetterich [c,1], Thomas Opel [d], Natalia V. Pravikova [b], Michael Fritz [c], Alexey V. Lupachev [e], Frank Günther [c,f], Andrei G. Shepelev [g], Igor I. Syromyatnikov [h], Alexander N. Fedorov [h], Mikhail V. Zimin [i], Guido Grosse [c,j]

[a] Lomonosov Moscow State University, Department of Cryolithology and Glaciology, Faculty of Geography, 119991 Moscow, Russia
[b] Lomonosov Moscow State University, Department of Regional Geology and Earth' History, Faculty of Geology, 119991 Moscow, Russia
[c] Alfred Wegener Institute Helmholtz Center for Polar and Marine Research, Permafrost Research Section, 14473 Potsdam, Germany
[d] Alfred Wegener Institute Helmholtz Center for Polar and Marine Research, Polar Terrestrial Environmental Systems Section, 14473 Potsdam, Germany
[e] Institute of Physicochemical and Biological Problems of Soil Science RAS, Laboratory of Soil Cryology, 142290 Pushchino, Russia
[f] Hochschule Neubrandenburg, Department of Landscape Sciences and Geomatics, 17033 Neubrandenburg, Germany
[g] Melnikov Permafrost Institute SB RAS, Laboratory of Permafrost Landscapes, 677010 Yakutsk, Russia
[h] Melnikov Permafrost Institute SB RAS, Laboratory of General Geocryology, 677010 Yakutsk, Russia
[i] Lomonosov Moscow State University, Department of Cartography and Geoinformatics, Faculty of Geography, 119991 Moscow, Russia
[j] University of Potsdam, Institute of Geosciences, 14476 Potsdam, Germany

ARTICLE INFO

ABSTRACT

Retrogressive thaw slumps (RTS) are an important landform of rapid permafrost degradation in regions with very high ground ice contents. RTS mobilize significant amounts of sediment, meltwater and organic carbon and impact downstream hydrological systems by directly affecting topography and water quality. The term mega-slump has previously been coined for RTS exceeding 20 ha in size. The Batagay megaslump in the Yana highlands of NE Siberia with an area of 87.6 ha (in 2023, including the bowl-shaped part and the erosional outlet) has been identified as the largest megaslump on Earth. We use very high resolution remote sensing from satellite data and drones, geological structure modeling, and field data to assess how much and what material is thawed and mobilized in the Batagay megaslump. The total volume of permafrost thaw and material loss from the Batagay RTS amounts to about 1 million m^3 per year. The material is by one third composed of thawed sediments and by two thirds of melted ground ice. About 4000 to 5000 tons of previously permafrost-locked organic carbon is released every year. Organic carbon content has been measured as Total Organic Carbon (TOC) of sediments and as Dissolved Organic Carbon (DOC) of ground ice. From its formation in the 1970s until 2023, the Batagay RTS – due to thermal denudation and headwalls retreat – mobilized a total volume of about 34.7 million m^3 of which 23.4 million m^3 were melted ground ice and 11.3 million m^3 were thawed deposits including a total of about 169,500 t organic carbon. With these rates of sediment and carbon mobilization, the Batagay megaslump is not only a prominent local feature of rapid permafrost thaw, but offers excellent conditions to study rates and mechanisms of rapid permafrost degradations and to calculate the stock and release of, e.g., organic matter.

1. Introduction

Modern climate warming, indicated by rising in air temperature and precipitation in the Arctic (IPCC, 2021), leads to changes in the temperature state of permafrost (Smith et al., 2022), an increase in the depth of seasonal thawing (Romanovsky et al., 2017), and activation of

processes associated with permafrost thawing (Zhang et al., 2022; Li et al., 2024). These geomorphological processes are widespread and result in mass movements leading to the mobilization of matter that has been preserved in the frozen state for a long time (Turetsky et al., 2020). These processes of permafrost degradation are highly dynamic and facilitate the transport of mobilized matter over significant distances (Lantuit et al., 2009; Littlefair et al., 2017; Zhang et al., 2022). Rapid permafrost thaw features are widespread and observed to increase in Arctic and sub-Arctic ice-rich permafrost terrain (e.g., Runge et al., 2022). Such intensification of permafrost degradation processes is linked to the changes of the Arctic hydrological and thermal regimes by warming, increased precipitation, and increased snow cover thickness, which induces deepening of the seasonally thawed (active) layer covering the permafrost (e.g., Douglas et al., 2021). In addition, natural and anthropogenic disturbances such as taiga and tundra fires (e.g., Yanagiya et al., 2023), coastal erosion (e.g., Nielsen et al., 2022), or technogenic disturbance of the land surface (e.g., Streletskiy et al., 2012) facilitate rapid permafrost thaw processes. One of the most common rapid permafrost disturbance features are retrogressive thaw slumps (RTSs), which are - if exceeding a surface area of 20 ha - considered as megaslumps (Lacelle et al., 2015).

The so-called "Batagay crater" or Batagay megaslump, whose growth emerging from a pre-existing hillslope ravine was firstly recognized on satellite imagery of 1991 (Kunitsky et al., 2013). Since then, average headwall retreat rates have been calculated for different sections of the feature, reaching 7 to 15 m per year (in 2004–2010; Kunitsky et al., 2013), 11.3 to 14.9 m per year (in 1991–2018; recalculated from area loss data given in Vadakkedath et al., 2020) and even up to 30 m per year (Günther et al., 2016). Additionally a few studies have been carried out to project the RTS's further growth (Matchitov et al., 2022).

Previous results of an unmanned aerial vehicle (UAV) survey and of laboratory data on ice and sediment composition obtained in 2019 allowed a characterization of the volumetric ice content distribution of the exposed cryolithological horizons in the largely vertical RTS headwalls and to identify the main morphological features of the landforms on the RTS floor as well as the headwall's morphology (Kizyakov et al., 2023).

The study of the Batagay RTS provides insights into drivers and processes of rapid permafrost thaw possibly predefined by cryolithological (permafrost) properties such as ice content, horizon thickness, and material parameters, which control the morphology and the expansion (headwall retreat) rates of the RTS.

As a result of processing of UAV imagery of 2019 and 2023 as well as stereo-pairs of satellite images of 2014, a series of digital surface models (DSMs) was constructed that characterizes the successive stages of three-dimensional (3D) expansion of the Batagay RTS, i.e., headwall retreat and deepening of the RTS floor.

This study presents the results of 3D geological modeling that unravels the cryolithological subsurface structure of the key-site and an assessment of thawed-sediment and meltwater fluxes during the RTS growth since initiation. As fluxes we consider only the mobilization of material that was preserved in a frozen state, and then thawed and moved from its location in a permafrost sediment section. This release of material is associated with thermal denudation of ice-rich deposits and RTS's headwalls retreat. We do not consider the end point of the fluxes and the final receiving basin. It is obvious that part of the material released with thermal denudation can be retained for long of short times, in various parts of transportation route, such as at the RTS floor, along the length of a thermal-erosional ravine, and can also be deposited in the alluvial accumulation of the Batagay River valley. By linking on-site observations, laboratory analyses, and satellite and UAV imagery products the present study aims to (i) identify major controls on degradation pattern and intensity of the Batagay RTS, (ii) calculate the flux budgets of sediment, organic carbon, and ground ice, and (iii) to deduce the temporal pattern of sediment, organic carbon, and meltwater fluxes for the observation period in three time steps: (1) since formation

of the RTS to 2014, (2) from 2014 to 2019, and (3) from 2019 to 2023.

2. Study area

The Batagay thaw slump near the settlement of Batagay is located in the Yana Uplands of interior Yakutia (north-eastern Siberia, 67.58°N, 134.77°E) on the east-facing hillslope of the saddle between Mount Kirgillyakh (590 m above sea level; a.s.l.) and Mount Khatyngnakh (380 m a.s.l.; Fig. 1). The climatic conditions are strongly continental as seen in low mean annual precipitation (MAP) of 203 mm (1988–2017) and high annual air temperature amplitudes between −40 °C in winter (mean Dec–Feb) and 13.7 °C in summer (Jun–Aug). The mean annual air temperature (MAAT) is −12.4 °C (period 1988–2017; Murton et al., 2023). Since 1950, the MAAT has increased by >2 °C and the MAP by >50 mm (Savvinov et al., 2018). The continuous permafrost of the region reaches ~300 to 500 m deep with mean annual ground temperature between −9 and −7 °C at the 10–14 m, which is the depth of zero annual amplitude (Geocryological Map of the USSR, 1996).

In the western part of the Batagay RTS, the headwall rises up to about 55 m above the slump floor, exposing six cryostratigaphic horizons of ancient permafrost deposits (Murton et al., 2022). From floor to top, the lowermost exposed horizon is the Lower Ice Complex (Marine Isotope Stage (MIS) 16 or earlier) overlain by the Lower Sand horizon (some period between MIS 16 and 6). In the top part of the Lower Sand, the Reddish layer is a well-recognized lithological boundary on the imagery. For the sediment flux assessment it was interpreted as part of the Lower Sand horizon. The overlying Woody Layer (presumably a paleosol) includes lenses of woody material of paleo-erosional cuts (MIS 5; discontinuously distributed, in places present as up to 3 m thick lenses). The upper horizons are the Upper Ice Complex (MIS 4–2), the Upper Sand Unit (MIS 3–2) and the Holocene Cover on top (MIS 1). Previous research addressed various paleo-aspects of the Batagay permafrost archive (e.g., Ashastina et al., 2017a, 2018; Kienast et al., 2018; Murton et al., 2017, 2022; Opel et al., 2019a, b; Vasil'chuk et al., 2019, 2020; Courtin et al., 2022; Jongejans et al., 2022a), while the most recent overview is given in Murton et al. (2023).

Here, instead of using a cryostratigraphic division of the strata based on dating (Murton et al., 2023), we use a division into cryolithological horizons based on differences in cryogenic structure and, first of all, on volumetric ice content due to the presence of vast ice-wedges. This division inherits our approach published earlier (Kizyakov et al., 2023) and is most consistent with the task to calculate the erosional budgets of sediment and meltwater fluxes.

In the following, we will use the "Batagay site", meaning the portion of the slope surrounding the RTS, the subsurface structure of which we are modeling and discussing as an extrapolation of data on the 3D position of the boundaries of the cryolithological horizons exposed in the RTS.

3. Materials and methods

3.1. Fieldwork

In spring 2019, frozen sediment samples were acquired by continuous sampling along the ~55 m deep western headwall on climbing rope and complemented by additional sampling sites on the slump floor and slopes (Jongejans et al., 2021; Jongejans et al., 2022a); covering the entire exposed cryolithological inventory (Table 1). Airborne imagery was obtained in 2019 from UAV surveys using a DJI Phantom 4 Advanced drone (with 1-in. 20 megapixel CMOS sensor and f/2.8 wide-angle lens) (Kizyakov et al., 2023). Further fieldwork has been undertaken in spring 2020 to drill cores of permafrost deposits from the close surroundings of the Batagay thaw slump. These cores have been used to identify the depth of boundaries between the single cryolithological horizons in addition to the estimates from the exposures within the slump. The depth of borehole 3–20-B was 32.4 m, and those of borehole
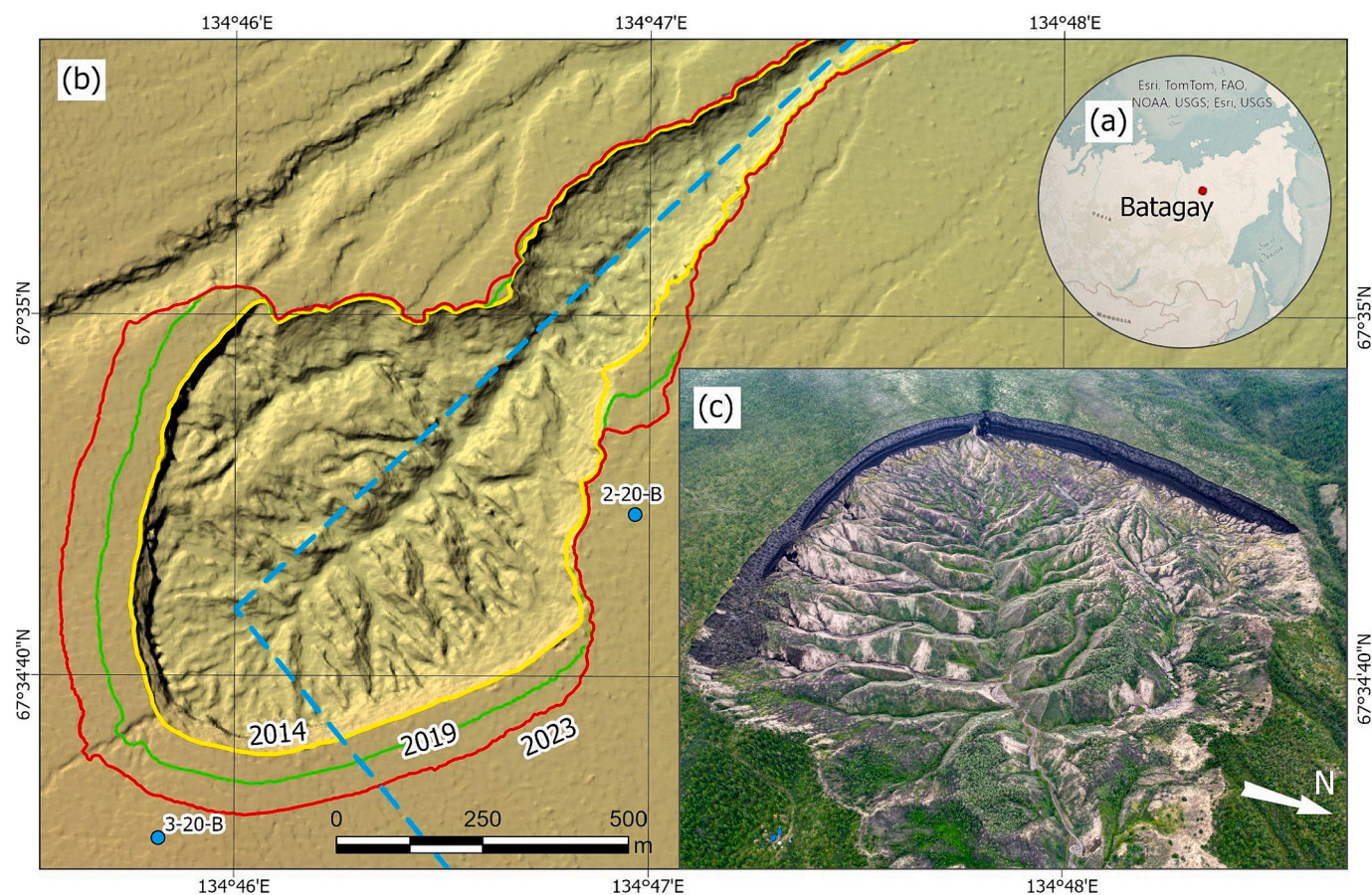
Fig. 1. Location of the Batagay RTS key-site (a) in Eastern Siberia, its topography (b) based on a DSM from 2014. The yellow, the green and the red lines delineate the RTS extent, based on satellite and UAV imagery, in 2014, 2019 and 2023. The blue dashed line delineates the location of the cross-section, presented in Fig. 5. The locations of boreholes drilled in 2020 are shown as blue points. The aerial view shows (c) the RTS at the end of July 2023 (oblique aerial image by A. Lupachev). (For interpretation of the references to colour in this figure legend, the reader is referred to the web version of this article.)

Table 1
Median values of quantitative characteristics of the cryolithological horizons, that were used in the 3D geological model. Initial sample data are given in Table S1. VICS – volumetric ice content, WIV – wedge-ice volume, sed + ice – sediment and intrasedimental ice, n/a – not analyzed.

Cryo- lithological horizon	Material	VICS	WIV	DOC [kg m^{-3}]	TOC [kg m^{-3}]	Summarized organic carbon content per horizon [kg m^{-3}]	Sand [%]	Silt [%]	Clay [%]
Cover Layer	sed + ice	0.5	n/a	0.1069	9.3	4.7035	56	37	7
Upper Sand	sed + ice	0.508	0.076	n/a	19.2	8.7285	17	77	6
Upper Ice Complex	sed + ice	0.564	n/a	0.3461	17.943	2.7373	47	47	6
	wedge ice	n/a	0.66	0.0168	n/a		n/a	n/a	n/a
Woody Layer	sed + ice	0.469	0.093	0.4309	26.1	12.7538	49	46	5
Lower Sand	sed + ice	0.469	0.093	0.2021	10.831	5.3023	54	42	4
Lower Ice Complex	sed + ice	0.532	n/a	0.7157	11.295	2.5611	55	40	5
	wedge ice	n/a	0.55	0.0201	n/a		n/a	n/a	n/a

2–20-B was 73.6 m (Fig. 1). In borehole 2–20-B, bedrock was found at a depth of 71.4 m below surface and we used this information to model the top of bedrock. In summer 2023, new airborne imagery was obtained from UAV surveys using a Mavic mini 3 pro with 1/1.3-inch 48 mega-pixel CMOS sensor and f/1.7 wide-angle lens.

3.2. Laboratory determination of sample properties

To determine the total volumetric ground ice content (TVIC) of each exposed cryolithological horizon, the wedge-ice volume (WIV) and the volumetric ice content (VICS) of sediments between ice wedges were determined as described in Kizyakov et al. (2023) using Eq. (1) after Grechishchev and Shur (1990):

$$\text{TVIC} = \text{WIV} + \text{VICS} \times (1 - \text{WIV}) \qquad (1)$$

The WIV was calculated based on its visible proportion in the headwall in a series of UAV imagery taken perpendicular to the headwall from the middle of its height, while the intrasedimental ice content (W_{tot}) was determined on 77 frozen samples as the gravimetric ice content by measuring the difference in weight percentage (wt%) between wet (frozen) and dry weights after freeze-drying (Zirbus Sub-liminator 3–4–5). To calculate the volumetric ice content of sediments between ice wedges (VICS), we used the Eq. (2) after Tsytovich (1973) and Grechishchev and Shur (1990) assuming the dry sediment density

(ρ) of 1500 kg m^{-3} (Tsytovich, 1973), the ice density (ρ_i) of 917 kg m^{-3} (Harvey, 2019) and the moisture content due to unfrozen water (W_w) as 0.01 (Kizyakov et al., 2023):

$$VICS = \frac{\rho_d \times (W_{tot} - W_w)}{\rho_i \times (1 + W_{tot})}, \tag{2}$$

The grain-size distribution (GSD) of the freeze-dried sediments was determined by laser diffraction particle analyses (Malvern Mastersizer 3000), and further analyzed using Gradistat 8.0 software (Blott and Pye, 2001) for sand-silt-clay distribution and arithmetic mean grain size in μm. In the following, sediments with grain-size of 2000 to 63 μm are considered as sand, 63 to 2 μm as silt, and < 2 μm as clay. Further details of GSD sample preparation and laboratory procedures are given in Schirrmeister et al. (2020). Total organic carbon (TOC) contents of 108 sediment samples were measured with the elemental analyzer Ele-mentarVario MAX C for TOC (analytical accuracy ±0.1 wt%; Jongejans et al., 2022a). Additionally, we included previously published TOC data (39 samples) from several cryolithological horizons (Table S1) (Ashas-tina et al., 2017a, 2017b; Jongejans et al., 2022b; Opel et al., unpublished 2017 data). The concentrations of dissolved organic carbon (DOC) in intrasedimental ice of the frozen deposits and in wedge ice were derived from 36 samples and 47 samples, respectively. After thaw of the frozen samples (or melt of the wedge-ice samples), meltwater was filtered in a glass filtration unit using pre-combusted glass fiber filters (Whatman GF/F; diameter: 47 mm, pore size: 0.7 μm). To prevent microbial conversion, the samples were acidified with HCl suprapur (30 %) to pH < 2. The DOC concentrations (mg L^{-1}) were measured with a high-temperature (680 °C) combustion total organic carbon analyzer (Shimadzu TOC-VCPH). The device-specific detection limit is 0.4 μg L^{-1}. Further details on DOC laboratory procedures are given in Wetterich et al. (2023).

The summarized organic carbon content within the cryolithological horizons, taking into account the content of organic carbon in the sediments, DOC in ice wedges and DOC in intrasedimental ice, was calculated as follows:

satellite imagery of 2014 (Günther et al., 2015). This DSM and the orthorectified image are used as reference. Using these reference datasets, a series ($n = 36$ for 2019 survey and $n = 42$ for 2023 survey) of reference control points (RCPs) were collected, which are distributed both within the RTS floor and on the surface of the slope outside the megaslump. RCPs were used at the stage of dense point cloud construction for co-registration of the aerial image orthomosaics of the spring 2019 and summer 2023 surveys. This spatial alignment of multi-temporal remote sensing data makes it possible to deduce the terrain changes between 2014, 2019 and 2023.

Based on the DSM of 2019, the slope terrain prior to the emergence of the thermal-erosional valley and the RTS formation was reconstructed. This surface was used as base topography in our 3D geological modeling of the cryolithological horizons structure at the site.

3.4. 3D geological modeling of the subsurface structure

We used the RTS model built in Agisoft Metashape with the original vertical and perspective drone images of the 2019 survey as a drape-over to identify the boundaries of cryolithological horizons (Fig. 2). Additionally, we used field observations of horizon positions from previous field surveys (Murton et al., 2017; Ashastina et al., 2017a; Opel et al., 2019a).

Within the RTS headwall, horizon boundaries are exposed along nearly 1.6 km length in the main part of the bowl-shaped RTS and additional outcrop fragments showing horizon boundaries are present on both sides of the northeastern erosional valley (Fig. 2). Based on all this available information on the traceable horizon boundaries, we reconstructed the 3D position of horizon boundaries at the Batagay site.

The shapefiles created in Agisoft Metashape with the 3D positions of the horizon's boundaries identified in the headwall exposures as well as from drilling and DSM data were used as a basis for geological modeling in the Petrel ver.2020.5 (Schlumberger software package).

We applied a standard workflow for the creation of the geological 3D model. Initial data for the 3D model creation were several DSMs and

$$\text{Summarized organic carbon content within horizon} = \left[\text{Sediments} \left(\text{TOC} + \text{DOC}_{\text{intrasedimental\_ice}}\right)\right] + \left[\text{Ice Wedges} \left(\text{DOC}_{\text{ice\_wedges}}\right)\right]$$
$$= \left[(1 - \text{WIV})^* \left(\text{DOC}_{\text{intrasedimental\_ice}}{}^* \text{VICS} + \text{TOC}^*(1 - \text{VICS})\right)\right] + \left[\text{WIV}^* \text{DOC}_{\text{ice\_wedges}}\right]. \tag{3}$$

To convert laboratory TOC and DOC data to volumetric content per cubic meter, the following equations were used:

$$\text{DOC} \left(\text{kg m}^{-3}\right) = DOC\left(\text{mg L}^{-1}\right)/1000, \tag{4}$$

$$\text{TOC per m}^3 = kg/m^3{}^* TOC(\text{wt\%}) = \left[1500^* TOC(\text{wt\%})\right]/100, \tag{5}$$

where the density of frozen sediments (ρ) used in calculations equals 1500 kg m^{-3} on average for sandy-silty sediments (Tsytovich, 1973).

3.3. Digital surface model computing

The RTS terrain characteristics were obtained as a result of processing airborne imagery from UAV surveys during the field campaigns 2019 and 2023. Vertical, nadir-looking aerial photography was used to derive the RTS topography. Oblique or horizontal looking aerial photography of the headwall was used to identify the position of the exposed cryolithological horizons. Image post-processing was undertaken using the Agisoft Metashape Professional ver.1.7.1 (Geoscan software package) to extract orthomosaics and digital surface models (DSMs).

Furthermore, a DSM was extracted from a stereopair of WorldView-1

surfaces that present the boundaries between strata as identified during field observation, from UAV data processing, and from drilling. The uppermost surface is the reconstructed DSM prior to RTS formation, i.e., representing an undisturbed slope surface before the initiation of the ravine and the RTS. Taking into account the more or less gentle topography of Batagay river valley and the absence of distinct variations in the thickness or altitude of the top and base of most of the identified horizons (with the exception of the Upper Sand) in exposures, these boundaries were initially approximated by surfaces close to the slightly inclined slope. Monocline surfaces have undergone minor manual correction to match with field data. The 3D model is a Corner Point Grid constructed using the Pilar Gridding method (Fremming, 2002). The first stage of modeling is the creation of the skeleton, which determines the limits and the planar geometry of the model cells. The dimensions of the key-site model are 2714 × 2690 m, divided into 1357 × 1345 cells. The average size of cells is 2 × 2 m and was deduced from the initial data resolution of the DSM of 2014. Further, the spatial relationships between the surfaces were entered, such as conformable, erosional cut or on lap. The model was then divided into vertical elements, a processing step called layering. We use 160 layers with a floating thickness from 0.1 to 2 m.

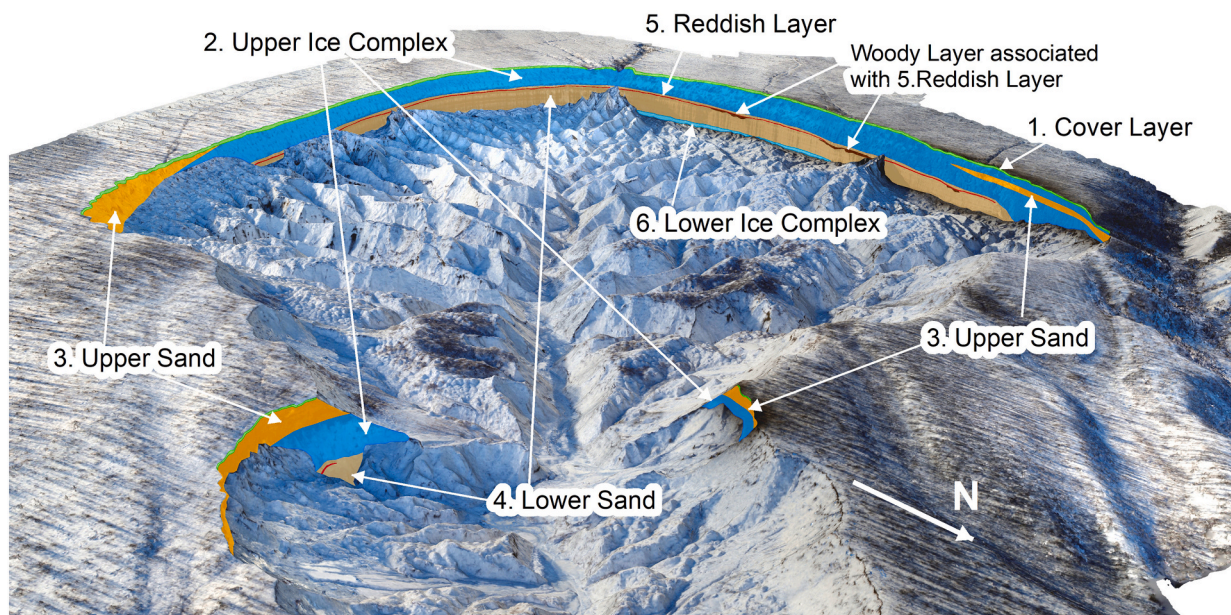During the property modeling, the quantitative geological

Fig. 2. Distribution of the cryolithological horizons and section elements on the headwall exposures of the Batagay RTS (see also Figs. 5, 6). The RTS terrain and image drape-over is based on a drone survey in spring 2019.

characteristics were defined. The cryolithological horizons are assigned with properties of sediment and ice-wedge samples that were determined in the laboratory (Table S1). As the sampling was localized mainly within one vertical profile and several additional points (Jongejans et al., 2022a; Kizyakov et al., 2023), for each horizon a median value was used to characterize its respective properties in the 3D model (Table 1).

3.5. Sediment and meltwater flux assessment

The total flux of sediment and meltwater associated with RTS expansion over time was calculated as the volumetric difference between the DSMs of 2014, 2019 and 2023. The resulting DEM difference is a per pixel assessment of the elevation difference and multiplied by the cell size represents the volumetric changes. The volume of deposits mobilized between the time steps represented by the DSMs was further differentiated by cryolithological horizons. Volume loss was calculated for each horizon. Based on earlier analysis of ice content distribution within the section (Kizyakov et al., 2023), the fluxes of solid sediments and meltwater were identified separately.

The differentiation of the sediment flux according to the

granulometric composition of sediments (sand, silt and clay) and carbon content was conducted in accordance with the properties of the horizons (Table 1). The ice/sediment ratio was calculated as a ratio of total volume of eroded material to the ice volume, expressed as a percentage.

The volume of the sediment flux was calculated in three time steps (1) from the beginning of the formation of an thermal-erosional ravine on the slope to 2014, (2) from 2014 to 2019, and (3) from 2019 to 2023. We acknowledge that these time slices are wide and do not allow to precisely assess the interannual variability of RTS volumetric growth, which could then be compared with meteorological data to establish clear relations of thermal denudation rates on finer temporal resolution. The volumetric difference between the 2014, 2019, 2023 DSMs, however, allowed us to make first-order estimates of the average annual sediment and meltwater fluxes for comparison with other RTS and areas of intense permafrost degradation.

The two intervals 2014–2019 and 2019–2023 have different durations in terms of warm season length, when the main growth of the RTS occurs. Thawing degree-days (TDD) were calculated as the sum of daily mean air temperatures (>0 °C) based on data from the Batagay meteorological station (Fig. 3; Weather schedule rp5.ru, n.d.). The 2019 field survey was taken at the end of March, thus it captures the state of the
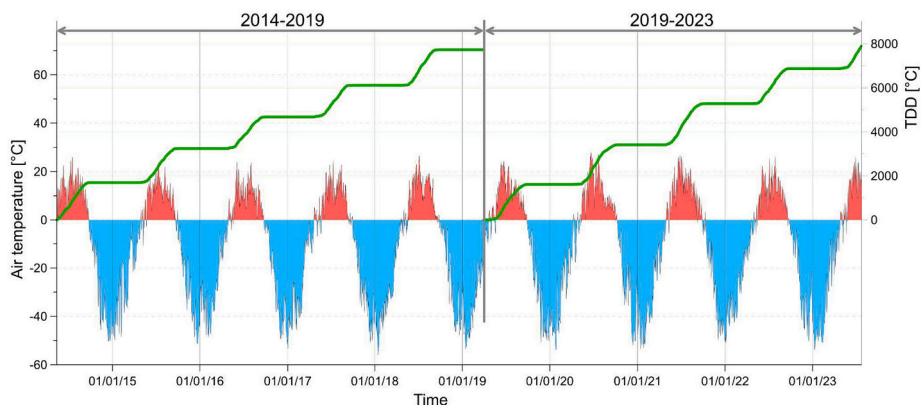

Fig. 3. Air temperature (above 0 °C filled by red, below 0 °C filled by blue) and cumulative thawing degree-days (TDD, as green line) at the Batagay RTS. (For interpretation of the references to colour in this figure legend, the reader is referred to the web version of this article.)

RTS at the end of the warm period of 2018. As the 2014 imagery originates from May 2014, the period 2014–2019 covers five warm seasons, including 691 days with an average daily temperature above 0 °C, amounting to TDD of 7730. The 2023 field survey was carried out in July, so the period 2019–2023 covers about 4.5 warm seasons, including 656 days with a positive average daily temperature and TDD was 7894. To calculate the average annual flux from the RTS, the volumetric values were divided by five (warm seasons) in the first case (2014–2019) and by 4.5 (warm seasons) in the second case (2019–2023).

4. Results

4.1. Batagay RTS growth in 2014–2023

The main changes in the RTS morphology since 2014 have been localized in the western, southern and southeastern parts, in particular at the headwalls with high ice content (mainly in the Upper Ice Complex). Thermal denudation led to an increase in both the RTS width and its length due to the intensive upslope growth. The maximum RTS width in 2014 was 790 m and reached 890 m in 2019. In summer 2023, the RTS was about 990 m wide and the upper slope headwall in the southwestern part was about 2700 m away from the RTS mouth at the Batagay river bank (Fig. 1). The multi-year average retreat along the headwall edge in the western, southern and southeastern parts was 56 m in 2014–2019, and 53 m in 2019–2023. While there are almost no spatial differences between retreat rates at these sites in a 2D view, significant variations were observed in the change in topography and, accordingly, in the RTS volumetric growth. The greatest volumetric changes are confined to the western and southwestern parts of the RTS (Fig. 4), where the highest headwalls are located, and cryolithological horizons are exposed down to the Lower Ice Complex. In the southern and southeastern parts, volumetric changes are smaller and decrease towards the eastern end of the bowl-shaped part of the RTS, accompanied by the flattening of the headwalls. There is a narrow strip closely along the RTS western, southern and southeastern headwalls with relatively

little elevation change between 2019 and 2023, this is due to the profile of the retreating walls with a slight gentle part at the top. The greatest influence of inclined walls is observed in the southeastern part of the RTS. An increase in the width of the gentle sloping headwalls is observed in the southeastern part of the RTS.

In the area where the bowl-shaped RTS part transforms into the northeastern erosional valley, on both sides there are steep retreating headwalls. The multi-year average retreat along the headwall edge on the northern site of the valley was 9 m in 2014–2019, and 11 m in 2019–2023, while the length of the retreating headwall remained the same. On the second site located on the southeastern side of the valley, the length of the retreating walls from 2014–2019 to 2019–2023 decreased by almost twice, and the average value of the headwall retreat for these periods was 39 m and 30 m, respectively.

In addition to the volumetric changes associated with the lateral retreat of the subvertical headwalls, volume loss also occurred within the RTS floor. These changes were associated with (1) thaw subsidence of remnant ice-rich deposits, (2) sliding and gravitational displacement of material on the ridges at the RTS floor due to the erosional cut of the slope base, and (3) erosional washout of sediments on the sides and bottoms of ravines. An area with significant changes was noted in the places with baydzherakh (thermokarst mounds) presence within the elevation limits of the Upper Ice Complex distribution. It should be noted that within the RTS floor, significant (>1 m) changes in amplitude are occurring locally. The main area of the RTS floor was rather stable with elevation changes not exceeding 1 m, which we considered as the uncertainty threshold below which changes were filtered out due to the resolution of the DSMs used.

4.2. 3D geological model of the Batagay RTS

Our 3D model of the Batagay site includes the upper part of the slope, consisting of Quaternary permafrost deposits down to the top of the bedrock. For the underlying bedrock layer only the upper 20 m are shown for visualization purposes (Fig. 5). Based on the model results,
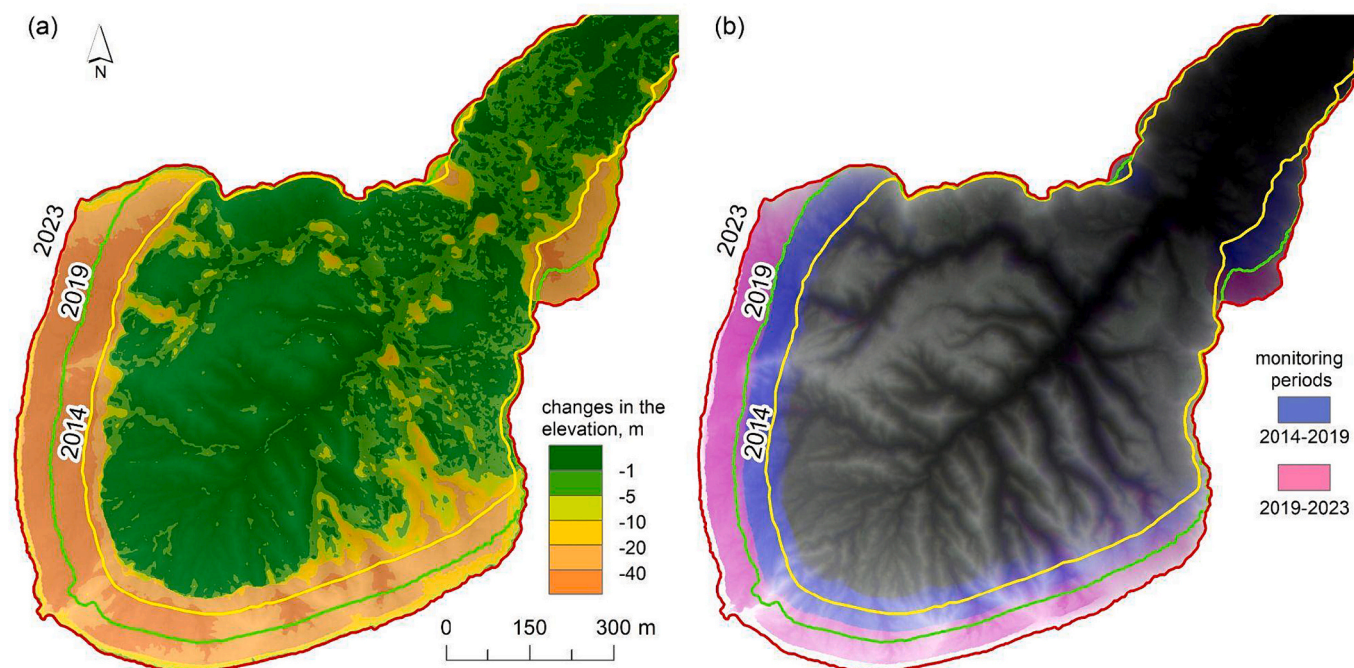

Fig. 4. Changes in elevation due to Batagay RTS growth (a), calculated as DSMs 2014 and 2023 difference. Growth by periods (b), represented as a RGB composite showing the difference between the 2019 and 2023 DSMs in purple and between 2014 and 2019 in blue. Saturated colors mark the areas with significant changes in topography in the respective periods. Lines delineating the RTS extent correspond to the Fig. 1 caption. (For interpretation of the references to colour in this figure legend, the reader is referred to the web version of this article.)
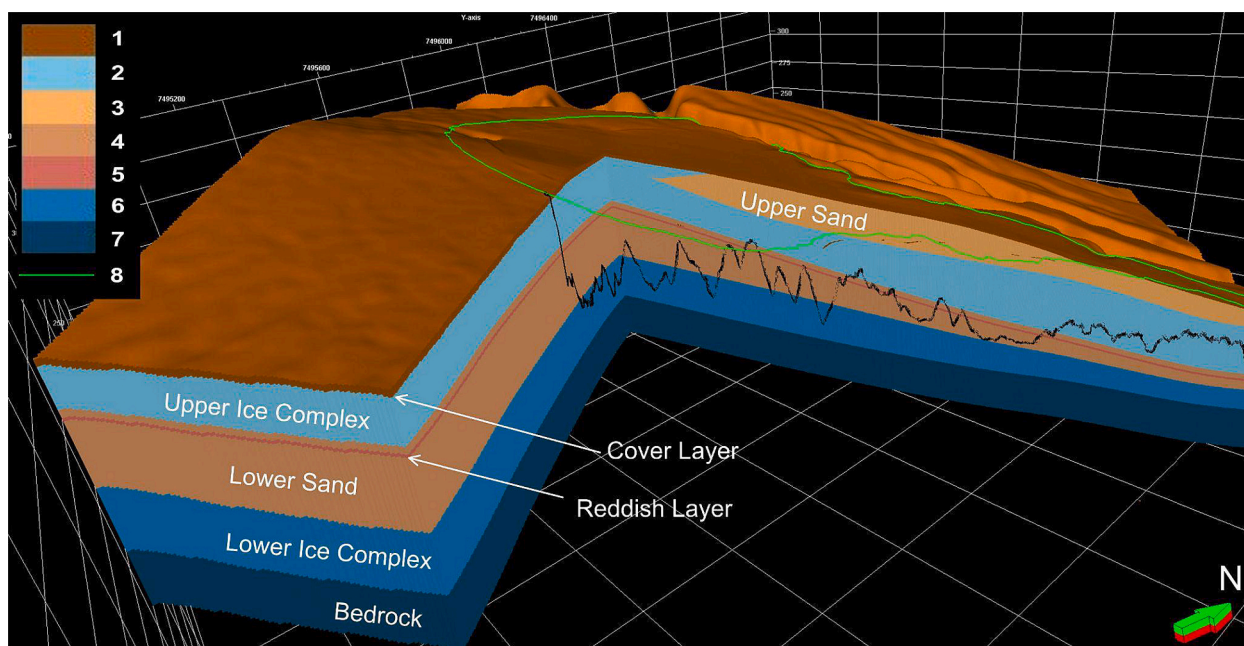
Fig. 5. Subsurface structures and positions of the cryolithological horizons of Batagay RTS: 1 – Cover Layer, 2 – Upper Ice Complex, 3 – Upper Sand, 4 – Lower Sand, 5 – Reddish Layer, 6 – Lower Ice Complex, 7 – Bedrock, 8 – Contour of the Batagay RTS in 2019. The black line on the cross section planes in the diagram delineate the RTS topography of 2019 along the cross section.

the thickness of each cryolithological horizon was obtained (Fig. S1). The Cover Layer has a constant thickness of 2 m, measured from the DSM, characterizing the mountain slope "before the RTS". Below the Cover Layer, due to the spatial variability of the cryolithological structure of the site, either the Upper Ice Complex or the Upper Sand is located in different parts of the slope.

In the northwestern part of the RTS, the Upper Ice Complex is dissected into two sub-horizons, which are divided by "sandwiched" deposits aligned with the Upper Sand. During modeling, the top of the Upper Ice Complex was specified as the base of the Cover Layer, which follows the key-site topography with its variability, therefore the top of the Upper Ice Complex varies in height, and the thickness of the horizon is reduced (completely washed out) within the erosion ravines in the northeastern part of the site. This horizon is exposed over a large extent of the RTS headwalls and its thickness varies both in the exposure and in the permafrost cores. In the 3D model, the average thickness of the Upper Ice Complex is 20–25 m (ranging from 16 to 27 m in different parts of exposed headwall) (Fig. S1a).

The Upper Sand horizon partly arises within the Upper Ice Complex, increasing its thickness from 0 m to 20 m, which is recorded in a fragmentary outcrop in the northeastern part of the RTS (Fig. S1b). Local reductions in the thickness of the horizon to 0 m in the northeastern part of the site are associated with erosional ravines that affect the geometry of the Upper Sand top, because here the Upper Sand is directly covered by the Cover Layer that follows the surface topography.

The thickness of the Lower Sand decreases towards the Batagay river valley from 28 to 8 m (Fig. S1c). This trend of cryolithological horizon thinning is based on observations of horizon thickness changes in the RTS headwalls.

The Lower Ice Complex in the RTS headwalls was exposed at the time of the survey only to a height of about 1.5 m. To model its thickness, we started from (a) the geometry of its top, slightly inclined to the northeast, according to measurements of the outcrop in the RTS headwalls, (b) the general trend of reduction in the thickness of all Quaternary permafrost horizons to the northeast, (c) depths of the bedrock top according to permafrost cores and observations of eluvium, being fragments of bedrock in the bottom of erosional ravines at the RTS floor, and (d) assumptions about the concave shape of the profile of the bedrock

top, which is exposed on the slopes and on the saddle between the mountains Kirgillyakh and Khatyngnakh, as well as at the bottom of the Batagay river valley. Based on these data and considerations, the thickness of the Lower Ice Complex decreases from 22 to 10 m to the northeast in the 3D model (Fig. S1d).

4.3. Sediment and meltwater fluxes

The combination of DSM data from different periods and the 3D geological model of the subsurface structure allows to calculate the volumetric loss of thawed deposits and meltwater differentiating between the cryolithological horizons, and over time (Fig. 6). Even though the distinct year of initiation of the RTS was most likely some time between 1980 and 1991 based on available remote sensing data, RTS growth of recent years is well represented by the present study. In detail, the time steps between May 2014 and March 2019 (five warm seasons; 2014–2019) and between March 2019 and July 2023 (four and a half warm seasons; 2019–2023) provide comparable yearly sediment and meltwater fluxes. Mean annual sediment fluxes are about 365,241 m^3 a^{-1} (2014–2019) and 307,668 m^3 a^{-1} (2019–2023). The mean annual meltwater fluxes amount to 745,081 m^3 a^{-1} (2014–2019) and 682,709 m^3 a^{-1} (2019–2023) (Table 2), which is about twice as much as the sediment flux. The mean combined volume loss of ice and deposits per year amounts to 1.11 million m^3 (2014–2019) and 0.99 million m^3 (2019–2023) (Table 2).

The largest contribution to volume loss is derived from the thickest exposed cryolithological horizons, i.e., the Upper Ice Complex and the Lower Sand. Given the prevalence of silt in the grain-size composition of all horizons, silt dominates the mineral material flux (Fig. 7). As the wedge-ice volume is highest in the Upper Ice Complex, it contributes the highest share of meltwater (from 52 to 61 %) to the total budget. The release of total organic carbon during the first period (2014–2019) is highest from deposits of the Lower Sand with up to 12,360 t, which is twice as high as from the Upper Ice Complex during the same period (6190 t). For the second period (2019–2023), the thawing of the Lower Sand mobilized 9930 t of organic carbon, compared to 6018 t from the Upper Ice Complex. The TOC content in the Upper Ice Complex sediments is almost equal to those in the Upper Sand (Table 1), but due to the
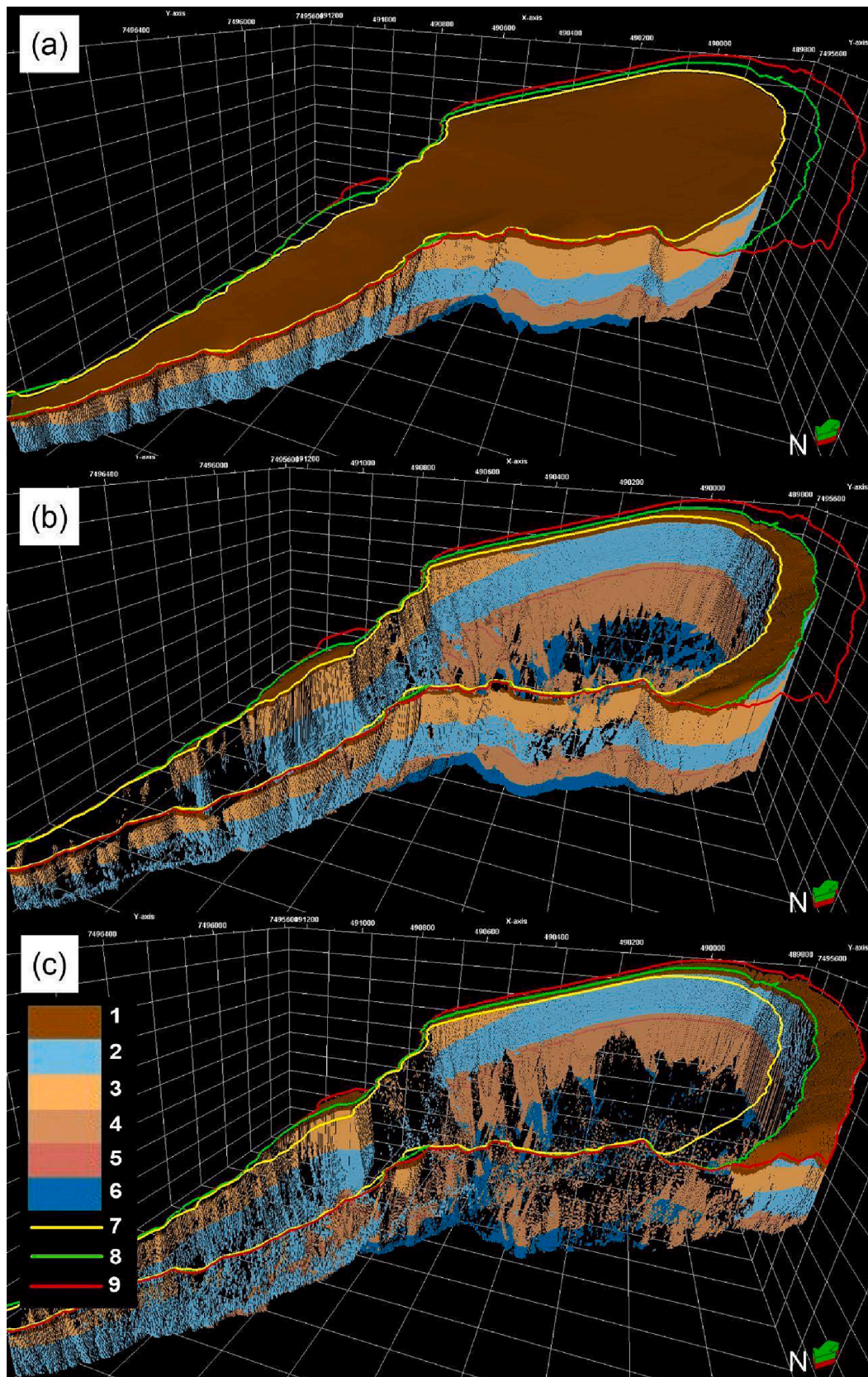
Fig. 6. Volumetric changes caused by RTS growth: (a) from the beginning of the formation of a ravine on the slope to 2014, (b) from 2014 to 2019, (c) from 2019 to 2023. 1 – Cover Layer, 2 – Upper Ice Complex, 3 – Upper Sand, 4 – Lower Sand, 5 – Reddish Layer, 6 – Lower Ice Complex, 7 – Contour of the Batagay RTS in 2014, 8 – Contour of the Batagay RTS in 2019, 9 – Contour of the Batagay RTS in 2023.

Table 2

Volume of material release calculations of the Batagay RTS in three time steps starting from the initiation of the RTS to 2014, from 2014 to 2019 and from 2019 to 2023. The organic carbon data comprise both TOC of sediments and DOC of ground ice.

| Cryolithological horizons	Total volume	Ice volume	Sediment volume	Sand volume	Silt volume	Clay volume	Organic carbon
	m³	m³	m³	m³	m³	m³	t
From the initiation of the RTS until 2014							
Cover Layer	1,116,046	558,023	558,023	312,493	200,888	39,062	5245
Upper Sand	5,944,961	3,245,949	2,699,012	458,832	2,078,240	161,941	51,900
Upper Ice Complex	10,096,754	8,622,628	1,474,126	692,839	692,839	73,706	27,665
Lower Sand	6,469,880	3,340,121	3,129,759	1,680,472	1 322,177	127,110	36,989
Lower Ice Complex	1,104,735	874,950	229,785	126,382	91,914	11,489	2828
Sum	*24,732,375*	*16,641,671*	*8,090,705*	*3,271,018*	*4,386,058*	*413,308*	*124,627*
From 2014 to 2019							
Cover Layer	196,598	98,299	98,299	55,047	35,388	6881	924
Upper Sand	618,969	337,957	281,012	47,772	216,379	16,861	5404
Upper Ice Complex	2,259,251	1 929,401	329,851	155,030	155,030	16,493	6190
Lower Sand	2,186,010	1,129,447	1,056,563	567,790	445,959	42,813	12,360
Lower Ice Complex	290,783	230,300	60,483	33,266	24,193	3024	744
Sum	*5,551,612*	*3,725,404*	*1,826,207*	*858,905*	*876,949*	*86,072*	*25,622*
Mean annual flux	*1,110,322*	*745,081*	*365,241*	*171,781*	*175,390*	*17,214*	*5124*
From 2019 to 2023							
Cover Layer	150,709	75,354	75,354	42,199	27,128	5275	708
Upper Sand	275,896	150,639	125,257	21,294	96,448	7515	2409
Upper Ice Complex	2,196,310	1 875,649	320,661	150,711	150,711	16,033	6018
Lower Sand	1,748,943	903,354	845,589	454,267	357,028	34,294	9930
Lower Ice Complex	84,839	67,192	17,646	9706	7059	882	217
Sum	*4,456,697*	*3,072,190*	*1,384,508*	*678,175*	*638,373*	*63,999*	*19,282*
Mean annual flux	*990,377*	*682,709*	*307,668*	*150,706*	*141,861*	*14,222*	*4285*
Total sum	*34,740,684*	*23,439,265*	*11,301,420*	*4,808,098*	*5,901,380*	*563,379*	*169,531*
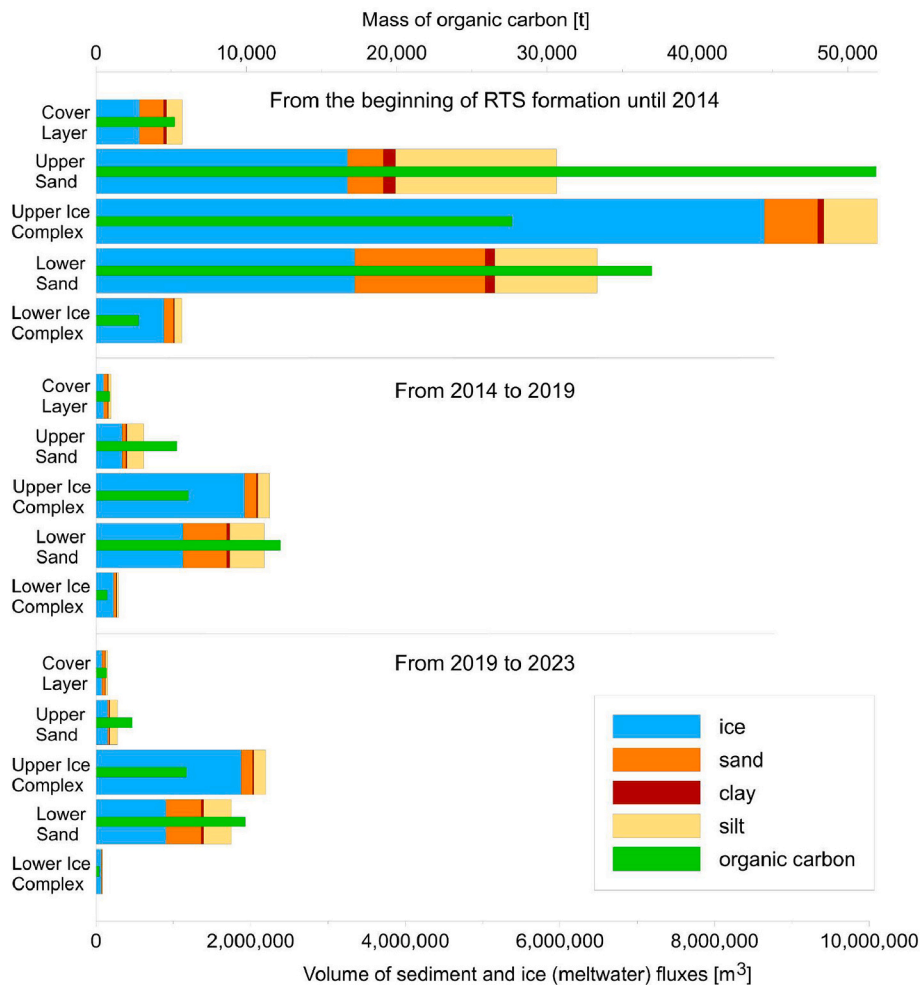
Fig. 7. Sediment, ice (meltwater) and organic carbon loss for the time periods (a) beginning of the RTS formation until 2014, (b) from 2014 to 2019, and (c) from 2019 to 2023 differentiated by the main cryolithological horizons of the Batagay RTS.
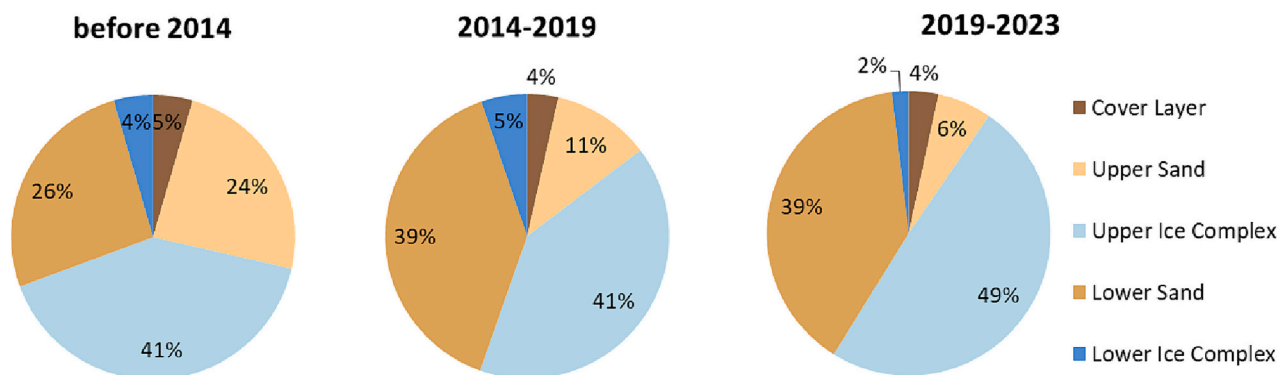
Fig. 8. Contribution of each cryolithological horizon to the total material flux for the periods before 2014, 2014–2019 and 2019–2023.

huge volume of ice wedges with low DOC contents, the Upper Ice Complex produces a smaller amount of summarized organic carbon flux in absolute values. The mean annual organic carbon flux from all horizons exposed at the Batagay RTS amounts to 5124 t a^{-1} in 2014–2019, and to 4285 t a^{-1} in 2019–2023.

The ratio between cryolithological horizons in the volume of material flux from the RTS changed over time due to the headwall retreating upslope and slump floor deepening in accordance with changes of the exposed geological structures (Fig. 8). Until 2014, the Upper Sand and Lower Sand units accounted for 50 % of the sediment flux volume, with approximately equal contributions. During 2014–2019, the portion of Upper Sand decreased from 24 to 11 %, while both Upper and Lower Sand still supplied 50 % of the total flux from the RTS. In 2019–2023, the portion of Upper Sand continued to decline to 6 %, and the portion of Upper and Lower Sand accounted for a total of 45 % of the flux.

Despite these changes in the volume ratio in the eroded cryolithological horizons, the ice/sediment ratio changed very little. Before 2014 and during the 2014–2019, the ice/sediment ratio was 67 %, and in 2019–2023 it was 69 %. This constancy is associated with the high TVIC of all cryolithological horizons (Kizyakov et al., 2023). Therefore, at the current stage of RTS growth, when all frozen deposits are exposed in the headwalls, spatial changes in the cryolithological structure around the headwalls and redistribution of flux volumes between these horizons did not lead to significant interannual changes in the ice/sediment ratio in flux.

5. Discussion

5.1. The effect of ground-ice distribution on RTS growth and morphology

5.1.1. Changes of ground-ice distribution in depth

The 3D geological model of the Batagay site was used for an assessment of the spatial distribution, thickness, and depths of the local cryolithological horizons and their effects on the growth dynamics of the RTS. During the RTS growth in width and deepening of the RTS floor, thermal denudation captured increasingly deeper cryolithological horizons, involving this material in the outflow. Since these horizons have different TVIC, and as the ratio of these horizons in the retreating walls changed over time, the ice and sediment ratio also changed. The most significant changes occurred in the early stages of RTS growth, when the floor deepened. At the present stage, when the height of the headwalls has almost reached its maximum, the change in the ice and sediment ratio is determined only by the spatial variability of the cryolithological structure and thermal denudation activation around the retreating headwalls. In Fig. 9, the change in this ice/sediment ratio for a vertical column with 1 m square area is shown. Two sections were chosen: (a) the upper part of the RTS, where no deposits of the Upper Sand are present (section 1), and (b) the lower part of the RTS, where deposits of the Upper Sand unit are present (section 2). The cumulative curves show

the volume of solid matter and ice yield during deepening of the RTS floor (Fig. 9). The graphs illustrate the variability of conditions that determine the possibility of intensified thermal denudation and changes in the volume of sediment flux depending on the presence of cryolithological horizons with varying ice content and thickness in the headwall exposure.

The most favorable conditions for deepening of the RTS floor and retreat of the headwall is the period of growth before a headwall cuts the base of the Upper Ice Complex. At this stage as the ratio of the Upper Ice Complex in the headwall increased, the ratio of ice in the total volume flux reached up to 81 %. The deficit of solid sediments leads to an intensive growth of the RTS landform both in depth and in width.

In section 1 (Fig. 9b), the most effective deepening and expansion of the RTS is associated with the rise of ice/sediments ratio and expected from the top to a depth of 23.2 m (the base of the Upper Ice Complex). In this depth range, with the deepening of the RTS floor, the sediment flux decreased, there was an acute deficit of solid sediments, which favored the rapid growth of the RTS, since practically nothing had to be removed from the foot of the retreating headwalls. Excess water during ground ice melting led to the formation of thermo-erosional ravines. A further thermal denudation deeper than the base of the Upper Ice Complex led to a gradual increase in the proportion of solid matter with depth. Nevertheless, it should be emphasized that deeper the ice/sediments ratio did not decrease below 65 %, although changes associated with the exposure of underlying horizons are observed. Even this minimum ice volume provides an excess of water sufficient to transport solid material out of the RTS.

In section 2 (Fig. 9c), at the initial deepening stages of the thermo-erosional ravine down to the depth of 18 m, the intensity of thermal denudation was limited by the comparably low ice content in the Upper Sand horizon. During further deepening and involving the ice-rich Upper Ice Complex horizon in the denudation, the ice/sediment ratio increased from 54 to 69 %, reflecting more favorable conditions for thermal denudation and RTS expansion.

5.1.2. Spatial variation in ground-ice distribution

Based on all available information, the Upper Sand horizon has a limited distribution along the Batagay river valley and disappears uphill, where it is replaced by the thickening Upper Ice Complex deposits (Murton et al., 2023). The upper boundary of the Upper Sand crosses the RTS and is marked in the headwall sections (Fig. 10a). The boundary is also seen in the modern topography of the RTS floor. To the southwest of the Upper Sand distribution boundary (i.e., upslope) towards the central headwall, the RTS floor is characterized, firstly, by terrain with low dissection (Kizyakov et al., 2023), and secondly, by a greater depth difference between the initial restored slope topography "before the RTS" and the modern topography (Fig. 10b). The significant ice content in this part of the key-site due to the presence of the ice-rich Upper Ice Complex and the absence of the relatively ice-poor Upper Sand
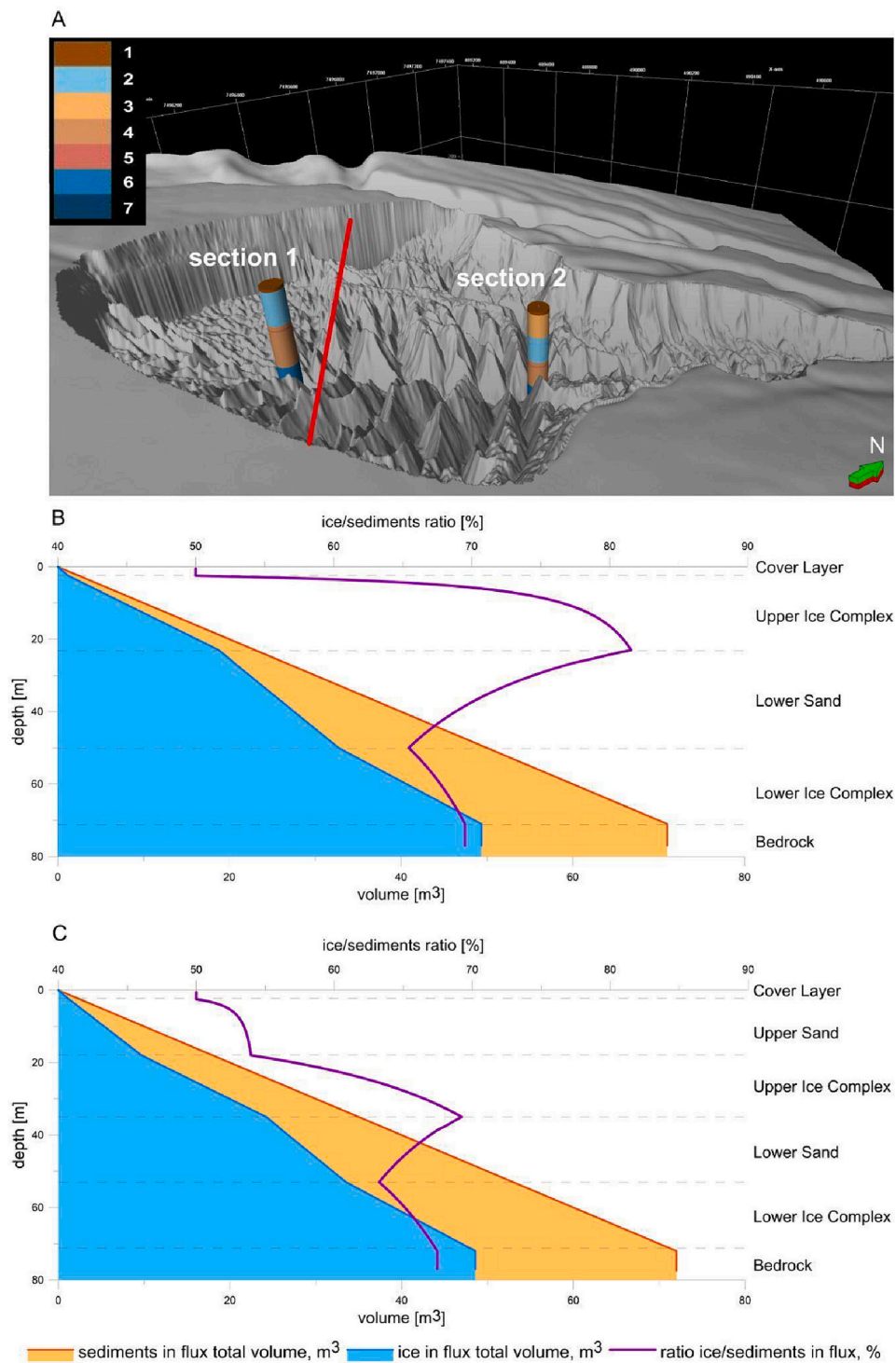
Fig. 9. Assessment of the flux changes in the ice/sediment ratio associated with the RTS floor deepening, depending on the section structure: (a) the location of test sections 1 and 2 on the axial position of the initial thermo-erosional ravine, the red line is the upslope limit of the Upper Sand distribution; the numbers correspond to the Fig. 6 caption; (b) section 1 without the Upper Sand horizons; (c) section 2 with the Upper Sand horizon. The Reddish layer is accounted as a part of Lower Sand. (For interpretation of the references to colour in this figure legend, the reader is referred to the web version of this article.)

promoted the transport of a larger volume of material out of the slump. In the northeastern part of the Batagay RTS with the Upper Sand horizon present, the floor deepening was less intense and selective. Here, in the floor topography, ridges are clearly expressed, which are built of material from the eroded Upper Ice Complex and still frozen material of the underlying strata. The ridges are separated by large V-shaped thermo-erosional ravines. The lower ice content of deposits exposed in this part of the key area (Fig. 9c), mainly due to much less WIV, caused a slowdown of the deepening below the base of the Upper Ice Complex, while cutting into the RTS floor occurred locally within the thermo-erosional ravines. These erosive landforms continuously deepened, especially at the recent stages of RTS growth, when excess water became available during the headwall retreat due to the higher ice content of the subsequently exposed horizons.
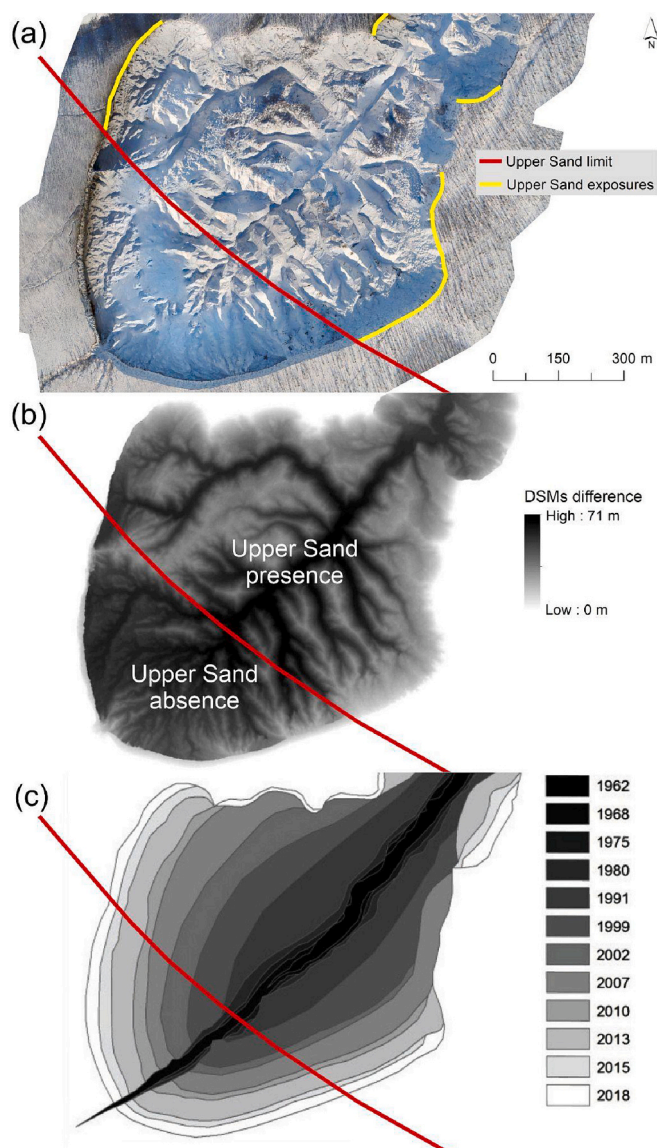
Fig. 10. Spatial distribution of the Upper Sand shown in (a) exposures of the Upper Sand in headwalls, fixed during field research and on drone imagery, (b) changes in RTS floor topography associated with Upper Sand limit, and (c) the stages of the RTS growth (redrawn from Savvinov et al., 2018).

Furthermore, the boundary of the Upper Sand distribution matches well the position of the headwall of the RTS in 1991, after which a change in morphology and intensified shape dynamics occurred as the RTS widened (Fig. 10c). From a typical linear thermo-erosional ravine, a bowl-shaped RTS emerged due to the growth in width resulting in an intensive area gain of the RTS (Kunitsky et al., 2013; Savvinov et al., 2018). We assume that this change in morphological dynamics precisely reflects the geological structure and stratigraphic heterogeneity of the Batagay site, in particular when the headwall of the thermo-erosional ravine passed the boundary of the Upper Sand distribution uphill and cut into the thick Upper Ice Complex deposits. The change in the morphological dynamics caused by the subsurface geological structure further promoted the increasing depth of the RTS floor, which most probably started in the second half of the 1990s although no DSM data is available from this period.

5.2. The Batagay RTS dimensions and dynamics in comparison

The amount of mobilized material of the Batagay RTS by permafrost

thaw and ground ice melt is exceptionally high and related to the huge dimension of this permafrost disturbance feature, the high ice content in at least two of its cryolithological structures, i.e., the Upper and the Lower Ice Complexes, and the resulting high retreat rates of the headwall. If compared to other known material fluxes from RTS of, e.g., the Canadian Arctic, the Batagay RTS characteristics seem to be outstanding.

Our data on the material flux and changes in topography, as well as data from other studies on the headwall retreat rates of the Batagay RTS, indicate that the RTS is still actively growing. When comparing the two periods 2014–2019 and 2019–2023, it turns out that the rate of thermal denudation, expressed in the RTS volumetric growth and the material flux, is slightly reduced. At the same time, as noted above, there were no changes in the ice/sediment ratio over the analyzed time periods. In the first period, the specific flux per 100 TDD was 71,800 m^3, and in the second period it decreased to 56,500 m^3. The reasons for this may be a decreasing length of retreating headwalls on the sides of the erosion outlet in 2019–2023, as well as a decrease in the retreat rate and flattening of the headwalls in the northwestern and eastern parts of the bowl-shaped part of the RTS (Figs. 4b, 6b, c), where the Upper Sand is present in the section (Fig. 10a).

RTS are widespread in the Arctic and sub-Arctic both in Eurasia and North America, where their locations are determined by permafrost properties and the late Pleistocene paleogeographic history of these regions. In Western Siberia massive (tabular) ground ice is formed through epigenetic freezing of marine Pleistocene deposits (Streletskaya and Leibman, 2003; Leibman et al., 2011). In the Canadian Arctic glacial legacies or postglacial freezing formed massive ice bodies (Bouchard, 1974; Fritz et al., 2011; Fritz et al., 2012). Areas with a long-term continental sedimentation regime in Eastern Siberia are characterized by the presence of ice-rich late Pleistocene permafrost such as the Yedoma Ice Complex (Schirrmeister et al., 2013) that represents the prerequisite for the occurrence of thermal denudation landforms, i.e., RTS.

In each of the regions where RTS are studied, their sizes vary significantly. In North America, a large number of active or stable RTS with a median size of 0.24 ha (mean of 1.52 ha) ranging from 20.81 ha to 0.01 ha were identified on the Yukon coast (Ramage et al., 2017). On Herschel Island in the northern Yukon Territory, the mean area of the largest, partly stabilized RTS, decreased due to coastal erosion in 1952–2000 from 6.2 to 3.3 ha (Lantuit and Pollard, 2008). For a single RTS on Herschel Island in 1970–2004 total volume of material loss was about 46,000 m^3 and sediment flux amounted to 10,600 m^3 per year (Lantuit and Pollard, 2008). On Banks Island in the Canadian High Arctic, the RTSs annual average area in 1984–2015 varied from 0.37 to 1.97 ha, with single RTS reaching up to 16 ha (Lewkowicz and Way, 2019). In the Richardson Mountains and Peel Plateau region, northwestern Canada, RTS area ranges from 0.4 to 52 ha (Lacelle et al., 2015), while the total disturbed area, consisting of the scar and the debris tongue, reaches 66.8 ha (Kokelj et al., 2015). RTSs larger than 5 ha (Kokelj et al., 2015) or larger than 20 ha (Lacelle et al., 2015) are also named as megaslumps.

In the Eurasian part of the Arctic on the eastern coast of Kolguev Island, RTS area varied from 0.4 to 8.3 ha in 2012 (Kizyakov et al., 2013). On the Yugorsky Peninsula several RTSs have been studied since 1999. Here, RTS areas in 2020 were within the range of 4 to 8 ha and the individual RTS area growth in 2010–2020 was within 0.04–0.3 ha per year (Leibman et al., 2021). On Central Yamal Peninsula, RTS in 2015 varied in area from 0.5 to 4.1 ha (Khomutov et al., 2017). On Taymyr Peninsula in 2010–2021 yearly area change per RTS increased up to 0.45 ha and yearly volumetric RTS growth increased up to 7700 m^3 (Bernard et al., 2022).

In most studies RTS growth dynamics are estimated by measuring headwall annual retreat rates. Published retreat rates range from several centimeters up to decameters per year for some RTS in Western Siberia, Eastern Siberia and Canada (Nesterova et al., 2024). In the Canadian

High Arctic on Eureka Sound Lowlands, Ellesmere and Axel Heiberg islands, maximum individual RTS (headwall) retreat rates reached 79 m per year in 2011–2018 (Ward Jones et al., 2019). These values obtained are very close to the maximum identified at Yugorsky Peninsula in the Western Siberia (Leibman et al., 2021).

It has been shown that RTS are a major contributor to lateral carbon fluxes along sea shores (Lantuit et al., 2009; Ramage et al., 2019; Ramage et al., 2018) and into freshwater ecosystems (Cassidy et al., 2016; Kokelj et al., 2013; Kokelj et al., 2015; Littlefair et al., 2017; Kokelj et al., 2021; Bernhard et al., 2022). The distance from the retreating headwalls to the receiving pool and the topography of the RTS floor determines the transport of the eroded material or the possibility of its partial re-deposition.

Given the arctic-wide distribution of RTS and a variety of local permafrost, climatic conditions, and topography, the Batagay RTS is currently the largest known distinct permafrost disturbance feature on Earth in both, its size and its annual flux volume. In 2023, the Batagay RTS with its erosional outlet to Batagay river bank covers an area of 87.6 ha (including the bowl-shaped part that covers 68.2 ha) that is the largest known extent for an RTS on Earth.

6. Conclusions

As a result of a joint analysis of the 2019 field datasets and previously published data, laboratory data of sediment and wedge ice composition, as well as UAV surveys in 2019 and 2023 as a base for imagery and a series of DSMs, we developed a 3D model of the subsurface structure of the Batagay RTS site. The model reflects the state-of-the-art understanding of the structure of the Quaternary deposits at the Batagay site.

Our 3D model includes data on the spatial distribution of cryolithological horizons and their variability in thickness as well as data on the composition of the horizons, including data on ice content, grain size distribution of sediments, and organic carbon content.

The 3D model allows a high accuracy assessment of material fluxes over time and the temporal evolution of the RTS. We specifically were able:

1. to estimate the volume of the sediment and meltwater fluxes from the RTS with the separation according to the cryolithological horizons;
2. to use a series of multi-temporal DSMs to analyze the variability of the RTS volumetric growth over time, in contrast to the existing estimates of the retreat of the RTS edges in a two-dimensional plane;
3. to evaluate the consistent involvement of various horizons in the sediment and meltwater fluxes. The deposits located at great depths were affected by thermal denudation and started being removed from the RTS only when the floor deepened significantly at the later stages of the RTS bowl-shaped landform formation;
4. to reveal that the ice/sediment ratio of mobilized material changed significantly during initial stages of RTS growth and deepening, caused by variation in ice content of the horizons, successively down from the daylight surface cut through by thermal denudation. On the current stage with a deep RTS floor cut, interannual changes in ice/sediment ratio in flux are less expressed due to the stable section composition around the headwalls. Keeping the very high ice/sediment ratio in flux, reaching up to 69 %, ensures the maintenance of high rates of RTS volumetric growth for several decades;
5. to conclude that further deepening of the RTS floor is limited by the location of the bedrock top a few meters below the current slump floor.

During 2019–2023, the Batagay RTS grew in length upslope, while simultaneously increasing the width of the bowl-shaped part, which reached 990 m in 2023. In the western, southern and southeastern parts, headwalls retreated by 53 m over 4.5 warm seasons, averaging almost 12 m per year. Additional sites with retreating headwalls on the sides of the northeastern erosional valley are of significantly less extent, but on the northeastern site they have retreated almost at the same rate.

Since initiation in the 1990s the Batagay RTS mobilized a total ground volume of ca. 35 million m^3, associated with headwalls retreat and floor deepening. After 2014 the annual mobilized volume amounts to ca. 1 million m^3 per year. Due to very high ice content, about $^2/_3$ of the total flux is melted ground ice and $^1/_3$ is thawed permafrost deposits. RTS growth leads to organic carbon release from 4000 to 5000 tons per year. In recent years, the Lower Sand has been the main organic carbon supplier.

For the future growth of the Batagay RTS, the possibility of further deepening has practically already been exhausted due to the underlying bedrock geology and only expansion along the margins and upslope is expected. However, this lateral expansion is also limited by the proximity of bedrock, the top of which apparently rises to the saddle between the mountains Kirgillyakh and Khatyngnakh about 550 m uphill of the megaslump.

CRediT authorship contribution statement

Alexander I. Kizyakov: Writing – original draft, Visualization, Investigation, Formal analysis, Conceptualization. **Maxim V. Korotaev:** Visualization, Software. **Sebastian Wetterich:** Writing – original draft, Investigation, Data curation. **Thomas Opel:** Writing – original draft, Data curation. **Natalia V. Pravikova:** Visualization, Software. **Michael Fritz:** Writing – original draft. **Alexey V. Lupachev:** Writing – review & editing, Resources. **Frank Günther:** Writing – original draft. **Andrei G. Shepelev:** Writing – original draft. **Igor I. Syromyatnikov:** Writing – original draft. **Alexander N. Fedorov:** Writing – original draft, Visualization, Investigation, Formal analysis, Conceptualization. **Mikhail V. Zimin:** Visualization, Software. **Guido Grosse:** Writing – review & editing, Funding acquisition.

Declaration of competing interest

The authors declare that they have no known competing financial interests or personal relationships that could have appeared to influence the work reported in this paper.

Data availability

All original analytical data of the study is given in Table S1.

thank Schlumberger Logelco Inc. for the Petrel software provided for education and research purposes at Lomonosov Moscow State University, Faculty of Geology.

Appendix A. Supplementary data

References

Ashastina, K., Schirrmeister, L., Fuchs, M., Kienast, F., 2017a. Palaeoclimate characteristics in interior Siberia of MIS 6–2: first insights from the Batagay permafrost mega-thaw slump in the Yana Highlands. Clim. Past 13, 795–818. https://doi.org/10.5194/cp-13-795-2017.

Ashastina, K., Schirrmeister, L., Scheidemann, D., Fuchs, M.C., Kienast, F., 2017b. Bulk Sedimentology of the Batagay Thaw Slump, Northeastern Siberia. PANGAEA. https://doi.org/10.1594/PANGAEA.877343.

Ashastina, K., Kuzmina, S., Rudaya, N., Troeva, E., Schoch, W.H., Römermann, C., Reinecke, J., Otte, V., Savvinov, G., Wesche, K., Kienast, F., 2018. Woodlands and steppes: Pleistocene vegetation in Yakutia's most continental part recorded in the Batagay permafrost sequence. Quat. Sci. Rev. 196, 38–61. https://doi.org/10.1016/j.quascirev.2018.07.032.

Bernhard, P., Zwieback, S., Hajnsek, I., 2022. Accelerated mobilization of organic carbon from retrogressive thaw slumps on the northern Taymyr Peninsula. Cryosphere 16, 2819–2835. https://doi.org/10.5194/tc-16-2819-2022.

Blott, S.J., Pye, K.A., 2001. GRADISTAT grain size distribution and statistics package for the analysis of unconsolidated sediments. Earth Surf. Process. Landf. 26, 1237–1248. https://doi.org/10.1002/esp.261.

Bouchard, M., 1974. Géologie des dépôts meubles de l'île Herschel, Territoire du Yukon. MSc thesis,. Université de Montréal, Montréal, Quebec, 70 p.

Cassidy, A.E., Christen, A., Henry, G.H.R., 2016. Impacts of active retrogressive thaw slumps on vegetation, soil, and net ecosystem exchange of carbon dioxide in the Canadian High Arctic. Arctic Science 3, 179–202. https://doi.org/10.1139/as-2016-0034.

Courtin, J., Perfumo, A., Andreev, A.A., Opel, T., Stoof-Leichsenring, K.R., Edwards, M. E., Murton, J.B., Herzschuh, U., 2022. Pleistocene glacial and interglacial ecosystems inferred from ancient DNA analyses of permafrost sediments from Batagay megaslump, East Siberia. Environ. DNA 4 (6), 1265–1283. https://doi.org/10.1002/edn3.336.

Douglas, T.A., Hiemstra, C.A., Anderson, J.E., Barbato, R.A., Bjella, K.L., Deeb, E.J., Gelvin, A.B., Nelsen, P.E., Newman, S.D., Saari, S.P., Wagner, A.M., 2021. Recent degradation of interior Alaska permafrost mapped with ground surveys, geophysics, deep drilling, and repeat airborne lidar. Cryosphere 15, 3555–3575. https://doi.org/10.5194/tc-15-3555-2021.

Fremming, N.P., 2002. 3D geological model construction using a 3D grid. In: 8th European Conference on the Mathematics of Oil Recovery (ECMOR VIII), 3–6 September 2002, Freiberg, Germany, cp-104-00001. https://doi.org/10.3997/2214-4609.201405917.

Fritz, M., Wetterich, S., Meyer, H., Schirrmeister, L., Lantuit, H., Pollard, W.H., 2011. Origin and characteristics of massive ground ice on Herschel Island (western Canadian Arctic) as revealed by stable water isotope and hydrochemical signatures. Permafr. Periglac. Process. 22, 26–38. https://doi.org/10.1002/ppp.714.

Fritz, M., Wetterich, S., Schirrmeister, L., Meyer, H., Lantuit, H., Preusser, F., Pollard, W. H., 2012. Eastern Beringia and beyond: late Wisconsinan and Holocene landscape dynamics along the Yukon Coastal Plain, Canada. Palaeogeogr. Palaeoclimatol. Palaeoecol. 319–320, 28–45. https://doi.org/10.1016/j.palaeo.2011.12.015.

Geocryological Map of the USSR, 1996. In: Yershov, E.D. (Ed.), Scale 1:2,500,000. State Cartographic Factory, Vinnytsia, Ukraine (in Russian).

Implementation of composition and structure of frozen ground in prediction of permafrost related geological hazards - Manual. In: Grechishchev, S.E., Shur, Y. (Eds.), 1990. Ministry of Geology of USSR, Moscow, Russia (79 pp. in Russian).

Günther, F., Grosse, G., Wetterich, S., Jones, B.M., Kunitsky, V.V., Kienast, F., Schirrmeister, L., 2015. The Batagay mega thaw slump, Yana Uplands, Yakutia, Russia: permafrost thaw dynamics on decadal time scale. In: Conference: PAST Gateways - Palaeo-Arctic Spatial and Temporal Gateways - Third International Conference and Workshop, Terra Nostra, 2015/1, pp. 45–46. https://epic.awi.de/id/eprint/38008/.

Günther, F., Grosse, G., Jones, B.M., Schirrmeister, L., Romanovsky, V.E., Kunitsky, V.V., 2016. Unprecedented Permafrost Thaw Dynamics on a Decadal Time Scale: Batagay Mega Slump Development, Yana Uplands, Yakutia, Russia. AGU Fall Meeting, 12–16 December 2016, San Francisco. abstract #GC33G-05. https://agu.confex.com/agu/fm16/meetingapp.cgi/Paper/186547.

Harvey, A.H., 2019. Properties of ice and supercooled water. In: Haynes, W.M. (Ed.), CRC Handbook of Chemistry and Physics, 95th edition. CRC Press, Boca Raton, FL.

IPCC, 2021. In: Masson-Delmotte, V., Zhai, P., Pirani, S.A., Connors, L., Péan, C., Berger, S., Caud, N., Chen, Y., Goldfarb, L., Gomis, M.I., et al. (Eds.), Climate Change 2021: The Physical Science Basis. Contribution of Working Group I to the Sixth Assessment Report of the Intergovernmental Panel on Climate Change. Cambridge University Press, Cambridge, UK.

Jongejans, L.L., Opel, T., Courtin, J., Meyer, H., Kizyakov, A.I., Syromyatnikov, I., Shepelev, A., Wetterich, S., 2021. Batagay Spring 2019. Reports on Polar and Marine Research, 749, pp. 155–210. https://doi.org/10.48433/BzPM_0749_2021.

Jongejans, L.L., Mangelsdorf, K., Karger, C., Opel, T., Wetterich, S., Courtin, J., Meyer, H., Kizyakov, A.I., Grosse, G., Shepelev, A.G., Syromyatnikov, I.I., Fedorov, A.N., Strauss, J., 2022a. Molecular biomarkers in Batagay megaslump permafrost deposits reveal clear differences in organic matter preservation between glacial and interglacial periods. Cryosphere 16, 3601–3617. https://doi.org/10.5194/tc-16-3601-2022.

Jongejans, L.L., Mangelsdorf, K., Karger, C., Strauss, J., 2022b. Alkane, Fatty Acid, Total (Organic) Carbon and Nitrogen Distribution in Ancient Permafrost Deposits at the Batagay Megaslump, East Siberia. PANGAEA. https://doi.org/10.1594/PANGAEA.950124.

Khomutov, A., Leibman, M., Dvornikov, Yu, Gubarkov, A., Mullanurov, D., Khairullinet, R., 2017. Activation of cryogenic earth flows and formation of thermocirques on Central Yamal as a result of climate fluctuation. In: Mikoš, M., Vilímek, V., Yin, Y., Sassa, K. (Eds.), Advancing Culture of Living with Landslides. World Landslide Forum 2017. Springer, Cham, Switzerland, pp. 209–216. https://doi.org/10.1007/978-3-319-53483-1_24.

Kienast, F., Ashastina, K., Troeva, E., 2018. Phylogeography of a west-Beringian endemic plant: an ancient seed of *Stellaria jacutica* Schischk. detected in permafrost deposits of the last interglacial. Rev. Palaeobot. Palynol. 259, 48–54. https://doi.org/10.1016/j.revpalbo.2018.09.012.

Kizyakov, A.I., Zimin, M.V., Leibman, M.O., Pravikova, N.V., 2013. Monitoring of the rate of thermal denudation and thermal abrasion on the western coast of Kolguev Island, using high resolution satellite images. Kriosf. Zemli (Earth Cryosphere). XVII 4, 36–47 (in Russian).

Kizyakov, A.I., Wetterich, S., Günther, F., Opel, T., Jongejans, L.L., Courtin, J., Meyer, H., Shepelev, A.G., Syromyatnikov, I.I., Fedorov, A.N., Zimin, M.V., Grosse, G., 2023. Landforms and degradation pattern of the Batagay thaw slump, Northeastern Siberia. Geomorphology 420, 108501. https://doi.org/10.1016/j.geomorph.2022.108501.

Kokelj, S.V., Lacelle, D., Lantz, T.C., Tunnicliffe, J., Malone, L., Clark, I.D., Chin, K.S., 2013. Thawing of massive ground ice in mega slumps drives increases in stream sediment and solute flux across a range of watershed scales. J. Geophys. Res. Earth Surf 118, 681–692. https://doi.org/10.1002/jgrf.20063.

Kokelj, S.V., Tunnicliffe, J., Lacelle, D., Lantz, T.C., Chine, K.S., Fraser, R., 2015. Increased precipitation drives mega slump development and destabilization of ice-rich permafrost terrain, northwestern Canada. Glob. Planet. Chang. 129, 56–68. https://doi.org/10.1016/j.gloplacha.2015.02.008.

Kokelj, S.V., Kokoszka, J., van der Sluijs, J., Rudy, A.C.A., Tunnicliffe, J., Shakil, S., Tank, S.E., Zolkos, S., 2021. Thaw-driven mass wasting couples slopes with downstream systems, and effects propagate through Arctic drainage networks. Cryosphere 15 (7), 3059–3081. https://doi.org/10.5194/tc-15-3059-2021.

Kunitsky, V.V., Syromyatnikov, I., Schirrmeister, L., Skachov, Y.B., Grosse, G., Wetterich, S., Grigoriev, M.N., 2013. Ice-rich permafrost and thermal denudation in the Batagay area (Yana Upland, East Siberia). Kriosf. Zemli (Earth Cryosphere) XVII (1), 56–58 (in Russian).

Lacelle, D., Brooker, A., Fraser, R.H., Kokelj, S.V., 2015. Distribution and growth of thaw slumps in the Richardson Mountains–Peel Plateau region, northwestern Canada. Geomorphology 235, 40–51. https://doi.org/10.1016/j.geomorph.2015.01.024.

Lantuit, H., Pollard, W.H., 2008. Fifty years of coastal erosion and retrogressive thaw slump activity on Herschel Island, southern Beaufort Sea, Yukon Territory, Canada. Geomorphology 95, 84–102. https://doi.org/10.1016/j.geomorph.2006.07.040.

Lantuit, H., Rachold, V., Pollard, W.H., Steenhuisen, F., Ødegård, R., Hubberten, H.-W., 2009. Towards a calculation of organic carbon release from erosion of Arctic coasts using non-fractal coastline datasets. Mar. Geol. 257 (1–4), 1–10. https://doi.org/10.1016/j.margeo.2008.10.004.

Leibman, M.O., Kizyakov, A.I., Lein, A.Yu., Perednya, D.D., Savvichev, A.S., Vanshtein, B.G., 2011. Sulfur and Carbon Isotopes within Atmospheric, Surface and Ground Water, Snow and Ice as Indicators of the Origin of Tabular Ground Ice in the Russian Arctic. Permafr. Periglac. Process. 22 (1), 39–48. https://doi.org/10.1002/ppp.716.

Leibman, M., Kizyakov, A., Zhdanova, Y., Sonyushkin, A., Zimin, M., 2021. Coastal retreat due to thermodenudation on the Yugorsky Peninsula, Russia during the last decade, update since 2001–2010. Remote Sens. 13, 4042. https://doi.org/10.3390/rs13204042.

Lewkowicz, A.G., Way, R.G., 2019. Extremes of summer climate trigger thousands of thermokarst landslides in a High Arctic environment. Nat. Commun. 10, 1329. https://doi.org/10.1038/s41467-019-09314-7.

Li, Y., Liu, Y., Chen, J., Dang, H., Zhang, S., Mei, Q., Zhao, J., Wang, J., Dong, T., Zhao, Y., 2024. Advances in retrogressive thaw slump research in permafrost regions. Permafr. Periglac. Process. 1-18 https://doi.org/10.1002/ppp.2218.

Littlefair, C.A., Tank, S.E., Kokelj, S.V., 2017. Retrogressive thaw slumps temper dissolved organic carbon delivery to streams of the Peel Plateau, NWT, Canada. Biogeosciences 14, 5487–5505. https://doi.org/10.5194/bg-14-5487-2017.

Zhang, T., Li, D., East, A.E., Walling, D.E., Lane, S., Overeem, I., Beylich, A.A., Koppes, M., Lu, X., 2022. Warming-driven erosion and sediment transport in cold regions. Nat Rev Earth Environ 3, 832–851. https://doi.org/10.1038/s43017-022-00362-0.

Matchitov, Yu. Ya, Gadal, S.J.-P., Danilov, Yu. G, 2022. Geomodeling of Evolution Processes of the Thermokarst Batagay Crater (Batagayka) Using GIS. Vestnik of North-Eastern Federal University, vol. 4 (28), 77–84 (in Russian). doi:10.25587/SVFU.2022.28.4.007.

Murton, J.B., Edwards, M.E., Lozhkin, A.V., Anderson, P.M., Savvinov, G.N., Bakulina, N., Bondarenko, O.V., Cherepanova, M.V., Danilov, P.P., Boeskorov, V., Goslar, T., Grigoriev, S., Gubin, S.V., Korzun, J.A., Lupachev, A.V., Tikhonov, A., Tsygankova, V.I., Vasilieva, G.V., Zanina, O.G., 2017. Preliminary paleoenvironmental analysis of permafrost deposits at Batagaika megaslump, Yana

Uplands, northeast Siberia. Quat. Res. 87, 314–330. https://doi.org/10.1017/qua.2016.15.

Murton, J.B., Opel, T., Toms, P., Blinov, A., Fuchs, M., Wood, J., Gärtner, A., Merchel, S., Rugel, G., Savvinov, G., Wetterich, S., 2022. A multimethod dating study of ancient permafrost, Batagay megaslump, East Siberia. Quat. Res. 105, 1–22. https://doi.org/10.1017/qua.2021.27.

Murton, J., Opel, T., Wetterich, S., Ashastina, K., Savvinov, G., Danilov, P., Boeskorov, V., 2023. Batagay Megaslump: a review of the permafrost deposits, Quaternary environmental history, and recent development. Permafr. Periglac. Process. 34 (3), 399–416. https://doi.org/10.1002/ppp.2194.

Nesterova, N., Leibman, M., Kizyakov, A., Lantuit, H., Tarasevich, I., Nitze, I., Veremeeva, A., Grosse, G., 2024. Review article: retrogressive thaw slump theory and terminology. Cryosphere. https://doi.org/10.5194/egusphere-2023-2914 preprint.

Nielsen, D.M., Pieper, P., Barkhordarian, A., Overduin, P., Ilyina, T., Brovkin, V., Baehr, J., Dobrynin, M., 2022. Increase in Arctic coastal erosion and its sensitivity to warming in the twenty-first century. Nat. Clim. Chang. 12, 263–270. https://doi.org/10.1038/s41558-022-01281-0.

Opel, T., Murton, J.B., Wetterich, S., Meyer, H., Ashastina, K., Günther, F., Grotheer, H., Mollenhauer, G., Danilov, P.P., Boeskorov, V., Savvinov, G.N., Schirrmeister, L., 2019a. Past climate and continentality inferred from ice wedges at Batagay megaslump in the Northern Hemisphere's most continental region, Yana Highlands, interior Yakutia. Clim. Past 15, 1443–1461. https://doi.org/10.5194/cp-15-1443-2019.

Opel, T., Murton, J.B., Wetterich, S., Meyer, H., Ashastina, K., Günther, F., Grotheer, H., Mollenhauer, G., Danilov, P.P., Boeskorov, V., Savvinov, G.N., Schirrmeister, L., 2019b. Stable Water Isotope Data of Ice Wedges at the Batagay Megaslump and the Adycha River, Including Other Siberian Ice-Wedge Sites for Regional Comparison. PANGAEA. https://doi.org/10.1594/PANGAEA.904105.

Ramage, J.L., Irrgang, A.M., Herzschuh, U., Morgenstern, A., Couture, N., Lantuit, H., 2017. Terrain controls on the occurrence of coastal retrogressive thaw slumps along the Yukon Coast, Canada. J. Geophys. Res. Earth Surf. 122, 1619–1634. https://doi.org/10.1002/2017JF004231.

Ramage, J.L., Irrgang, A.M., Morgenstern, A., Lantuit, H., 2018. Increasing coastal slump activity impacts the release of sediment and organic carbon into the Arctic Ocean. Biogeosciences 15, 1483–1495. https://doi.org/10.5194/bg-15-1483-2018.

Ramage, J.L., Fortier, D., Hugelius, G., Lantuit, H., Morgenstern, A., 2019. Distribution of carbon and nitrogen along hillslopes in three valleys on Herschel Island, Yukon Territory, Canada. CATENA 178, 132–140. https://doi.org/10.1016/j.catena.2019.02.029.

Romanovsky, V., Isaksen, K., Drozdov, D., Anisimov, O., Instanes, A., Leibman, M., McGuire, A.D., Shiklomanov, N., Smith, S., Walker, D., 2017. Chapter 4. Changing permafrost and its impacts. In: Arctic Monitoring and Assessment Programme (AMAP). Snow, Water, Ice and Permafrost in the Arctic (SWIPA); Summary for Policy-makers. Fairbanks, USA.

Runge, A., Nitze, I., Grosse, G., 2022. Remote sensing annual dynamics of rapid permafrost thaw disturbances with LandTrendr. Remote Sens. Environ. 268, 112752 https://doi.org/10.1016/j.rse.2021.112752.

Savvinov, G.N., Danilov, P.P., Petrov, A.A., Makarov, V.S., Boeskorov, V.S., Grigoriev, S. E., 2018. Environmental problems of the Verkhoyansky region. Vestnik of North-Eastern Federal University 6 (68), 18–33 (in Russian).

Schirrmeister, L., Froese, D., Tumskoy, V., Grosse, G., Wetterich, S., 2013. Permafrost and Periglacial Features | Yedoma: Late Pleistocene ice-rich syngenetic permafrost of Beringia. In: Elias, S.A., Mock, C.J. (Eds.), Encyclopedia of Quaternary Sciences, Second edition. Elsevier, Amsterdam, The Netherlands, pp. 542–552. https://doi.org/10.1016/b978-0-444-53643-3.00106-0.

Schirrmeister, L., Dietze, E., Matthes, H., Grosse, G., Strauss, J., Laboor, S., Ulrich, M., Kienast, F., Wetterich, S., 2020. The genesis of Yedoma Ice Complex permafrost – grain-size endmember modeling analysis from Siberia and Alaska. E&G Quaternary Sci J. 69, 33–53. https://doi.org/10.5194/egqsj-69-33-2020.

Streletskaya, I.D., Leibman, M.O., 2003. Cryogeochemical model of tabular ground ice and cryopegs formation at central Yamal, Russia. Proceedings of the Eighth International Conference on Permafrost, 2. Phillips M, Springman SM, Arenson LU (Eds.). Balkema: Lisse; 1111–1115.

Smith, S.L., O'Neill, H.B., Isaksen, K., Noetzli, J., Romanovsky, V.E., 2022. The changing thermal state of permafrost. Nat Rev Earth Environ 3, 10–23. https://doi.org/10.1038/s43017-021-00240-1.

Streletskiy, D.A., Shiklomanov, N.I., Nelson, F.E., 2012. Permafrost, infrastructure, and climate change: a GIS-based landscape approach to geotechnical modeling. Arct. Antarct. Alp. Res. 44 (3), 368–380. https://doi.org/10.1657/1938-4246-44.3.368.

Tsytovich, N.A., 1973. Mechanics of Frozen Soils (General and Applied). Publishing House High School, Moscow, Russia, 448 pp. (in Russian).

Turetsky, M.R., Abbott, B.W., Jones, M.C., Walter Anthony, K., Olefeldt, D., Schuur, E.A. G., Grosse, G., Kuhry, P., Hugelius, G., Koven, C., Lawrence, D.M., Gibson, C., Sannel, A.B.K., McGuire, A.D., 2020. Carbon release through abrupt permafrost thaw. Nat. Geosci. 13, 138–143. https://doi.org/10.1038/s41561-019-0526-0.

Vadakkedath, V., Zawadzki, J., Przeździecki, K., 2020. Multisensory satellite observations of the expansion of the Batagaika crater and succession of vegetation in its interior from 1991 to 2018. Environ. Earth Sci. 79, 150. https://doi.org/10.1007/s12665-020-8895-7.

Vasil'chuk, Y.K., Vasil'chuk, J.Y., Budantseva, N.A., Vasil'chuk, A.C., Trishin, A.Y., 2019. High-resolution oxygen isotope and deuterium diagrams for ice wedges of the Batagai yedoma, Northern Central Yakutia. Dokl. Earth Sci. 487, 975–978. https://doi.org/10.1134/S1028334X19080312.

Vasil'chuk, Yu.K, Vasil'chuk, J. Yu, Budantseva, N.A., Vasil'chuk, A.C., 2020. New AMS dates of organic microinclusions in ice wedges from the lower part of Batagay Yedoma, Yakutia. Dokl. Earth Sci. 490, 100–103. https://doi.org/10.1134/S1028334X20020154.

Ward Jones, M.K., Pollard, W.H., Jones, B.M., 2019. Rapid initialization of retrogressive thaw slumps in the Canadian high Arctic and their response to climate and terrain factors. Environ. Res. Lett. 14, 055006 https://doi.org/10.1088/1748-9326/ab12fd.

Weather schedule rp5.ru. n.d. Available online: https://rp5.ru/ [online accessed November 7 2023].

Wetterich, S., Kizyakov, A.I., Opel, T., Grotheer, H., Mollenhauer, G., Fritz, M., 2023. Ground-ice origin and age on Herschel Island (Qikiqtaruk), Yukon, Canada. Quat. Sci. Adv. 10, 100077 https://doi.org/10.1016/j.qsa.2023.100077.

Yanagiya, K., Furuya, M., Danilov, P., Iwahana, G., 2023. Transient freeze-thaw deformation responses to the 2018 and 2019 fires near Batagaika megaslump, Northeast Siberia. J. Geophys. Res. Earth Surf. 128, e2022JF006817 https://doi.org/10.1029/2022JF006817.